35th Symposium on Naval Hydrodynamics
Nantes, France, 8 July - 12 July 2024

Towards High-Fidelity Modelling of Cavitating flows

A. Madabhushi[1], F. L. Brandao[1], K. Alame[1], K. Mahesh[1,2]
([1] Aerospace Engineering and Mechanics, University of Minnesota, USA)
([2] Naval Architecture and Marine Engineering, University of Michigan, USA)

ABSTRACT

Cavitation occurs over varying physical regimes, ranging from inception to sheet–to–cloud transition. In the inception regime, the extent of cavitation is determined by a number of factors, among which the presence of non-condensable gas and the size distribution of free nuclei are primarily important. On the other hand, for sufficiently low ambient pressure, massive sheet cavities are formed which often undergo sheet-to-cloud transition altering the properties of the mixture medium significantly. The objectives of this paper are: (a) quantify the effect of gas on inception using a Gibbs free energy approach, (b) develop a polydisperse model to study the effect of nuclei size distribution on cavitation inception and (c) develop a compressible hybrid model to capture both sub-grid vapor nuclei and massive sheet cavity dynamics.

INTRODUCTION

Cavitation refers to the phase change from liquid to vapor when the pressure drops below the saturated vapor pressure. It is commonly observed in marine applications such as propellers and hydrofoils. The cavitation number σ (defined as $\sigma = \frac{p_r - p_v}{0.5\rho u_r^2}$, where p_r, p_v, ρ and u_r are a reference pressure, the vapor pressure, the liquid density and a reference velocity, respectively) characterizes the nature of cavitation, varying from the inception regime at higher sigma to fully developed cavitation as sigma decreases. In the inception regime, the vapor cavities remain small and occur intermittently. The frequency of cavitation events is determined by the presence of non-condensable gas as well as the size and concentration of free-stream nuclei. However, in the developed regime, vapor cavities grow significantly, leading to phenomena such as the sheet-to-cloud transition, re-entrant jet formation, and the formation of bubbly shocks. In this work, we focus on developing models for different cavitation regimes while incorporating the realistic effects of non-condensible gas and the size of free-stream nuclei.

Inception occurs in the regime of low void fractions where the compressible governing equations can be argued to reduce to the zero—Mach equations, which allow the use of the incompressible governing equations along with the same vapor volume fraction transport equation as the compressible equations. Most numerical studies of tip vortex cavitation in the incipient regime employ an Euler–Lagrange framework, where the liquid follows the incompressible Navier–Stokes equations and each bubble is tracked individually with the equations of motion coupled with the Rayleigh–Plesset equation for their size (Hsiao et al., 2003; Cheng et al., 2021). This approach can yield more details on the interactions of the nuclei and the tip vortex, at the extra cost of modeling the nuclei dynamics. Here, we use an extension to the model proposed by Brandao and Mahesh (2022) where vapor is treated as a passive scalar in a incompressible liquid. This extension assumes the vapor phase as a polydisperse distribution of bubbles divided discretely into bins of different sizes. The simulations are based on the experiments of Boulon et al. (1999). The goals of the present work are: (i) to demonstrate the capability of LES to simulate the complex flow field, and (ii) to study the tip vortex cavitation under different conditions.

Detecting sub-micron particles in liquids, experimentally, is a difficult process that makes it challenging to distinguish between homogeneous and heterogeneous nucleation. A well known approach to studying nucleation from a fundamental standpoint is classical nucleation theory (CNT) that dates back to Gibbs (1906), Volmer and Weber (1926), Farkas (1927), Becker and Döring (1935), and Zeldovich (1943). Comprehensive work on CNT can be found in Frenkel (1955), Skripov (1974), Carey (2020), and articles by Blake (1949), Bernath (1952), Cole (1974), Blander and Katz (1975), and Lienhard and Karimi (1981). CNT is a theoretical framework to describe the formation of clusters for a thermodynamically stable phase within a metastable parent phase. Stochasticity is central to the nucleation process since thermodynamic fluctuations are governed by the Boltzmann distributions. These fluctuations are what drive the system to reach

a thermodynamic state that momentarily breaches the activation energy barrier leading to a phase transition (Maeda, 2020). The liquid phase has to deposit excess energy to create the nucleus. Recent work approached simulations using molecular dynamics to model the inception and nucleation processes (Chen et al., 2019; Gao et al., 2021; Menzl et al., 2016). We approach CNT from a general Gibbs free energy description to study the behavior and transition from homogeneous nucleation to heterogeneous nucleation in the presence of contaminant gas (in the absence of a solid). An analytical expression for the critical radius, activation energy, and diameter of the initial bubble distribution, are derived as a function of gas content. The model captures the continuous variation of gas content within a bubble. The method recovers the homogeneous model for the limiting cases, such as pure liquid-vapor bubbles, and Blake's critical radius.

The homogeneous mixture model (HMM) is widely used to study fully developed cavitation. Here, the mixture of liquid and vapor is represented as a single entity, with the assumption that they are in thermodynamic equilibrium (Gnanaskandan and Mahesh, 2015; Bensow and Bark, 2010; Budich et al., 2018). HMM has been successful in capturing phenomena like re-entrant jet and bubbly shock formation during the sheet-to-cloud transition in flows over a wedge, (Gnanaskandan and Mahesh, 2015; Bhatt and Mahesh, 2020). However, achieving accurate results in the incipient regime requires the use of a fine mesh, which can be computationally expensive. Madabhushi and Mahesh (2023) developed a compressible multi-scale model to address this challenge where the large-scale vapor cavities are governed by an Eulerian transport equation and the sub-grid vapor bubbles are tracked in a Lagrangian sense using the novel *kR-RP* equation (k - constant parameter, R - bubble size and RP - Rayleigh–Plesset). The *kR-RP* equation was formally derived in terms of the local fluid pressure impacting the bubble. In this work, we extend the multi-scale model to account for hybridization, i.e., a consistent transition between the Eulerian and Lagrangian frameworks based on the ratio of vapor size to the computational cell size.

GIBBS FREE ENERGY MODEL

A Gibbs free energy approach is used to study the effects of gas content on cavitation nuclei. The model provides a smooth transition from homogeneous to heterogeneous nucleation events depending on the gas content of the fluid. Contrary to standard models which assume saturated gas and Blake's radius as the critical radius, we investigate different gas content that gives rise to different behaviors when considering undersaturated, saturated, and supersaturated cases. The Gibbs free energy of the system can be defined by the following expression:

$$G_{tot} = (p_\ell - p_g - p_v)V_g + \sigma_{\ell g}(A_{\ell g} + A_{sg}\cos\theta_Y) + n_g BT \ln\frac{p_g}{s(p_\ell - p_v^*)} + n_v BT \ln\frac{p_v}{p_v^*} + G_o(p_\ell, T, s)\,. \tag{1}$$

The first expression on the right-hand side of (1) is the total bulk free energy G_{bulk}, where p_ℓ, p_g, and p_v are the liquid, gas, and vapor pressure respectively, and V_g the volume of the gas bubble. The second term represents the total interfacial energy G_{int}, where $sigma_{\ell g}$ is the surface tension of the liquid-gas interface, $A_{\ell g}$ and A_{sg} are the liquid-gas and solid-gas surface area respectively, and θ_Y is Young's contact angle. The third term is attributed to the total chemical potential energy between the free gas in the entrapped air within the cavity and dissolved gas in the liquid phase, where n_g is the number of gas moles, B is the gas constant, and T the temperature, and s the gas saturation degree. The asterisk denotes the saturated state. The fourth term is attributed to the total chemical potential energy between the unsaturated and saturated vapor phases, where n_v is the number of vapor moles. The third and fourth terms can be combined into the term G_{chem}. The last term G_o is the free energy of the Wenzel state which is a constant for a given p_ℓ, T, and s at the reference state.

In order to find the equilibrium solution, we need to set $\delta G_{tot} = 0$. Assuming we have a spherical bubble, and no solid impurities, the reference equation (1) can be simplified into:

$$r^3 + \frac{2\sigma_{\ell g}}{(p_\ell - p_v)}r^2 - \frac{3n_g BT}{4\pi(p_\ell - p_v)} = 0\,, \tag{2}$$

where r is the bubble radius. Define the variable $f(n_g)$ as:

$$f(n_g) = 2\left(\frac{9n_g BT}{8\pi\sigma_{\ell g}}\right)\left[\frac{3}{4}\frac{(p_{\ell,cr} - p_v)}{\sigma_{\ell g}}\right]^2, \tag{3}$$

a non-dimensional number that measures the saturation degree. For a special case when $f(n_g) = 2$, one can recover Blake's critical radius, representing the saturated state. If $f(n_g) < 2$, we are in the under-saturated regime. In the limiting case where $f(n_g) = 0$, we have a pure liquid-vapor system. When $f(n_g)$ is greater than 2, it represents a super-saturated regime.

By solving for the cubic equation, we can find analytic expressions for a generalized critical bubble radius that takes into account the gas content. For the incipient case, we get the following expression:

$$\begin{aligned} r_{cr} &= \xi_{inc}(n_g)\frac{2\sigma_{\ell g}}{(p_v - p_\ell)} \\ &= \xi_{inc}(n_g)\, r_{cr,v} \end{aligned} \tag{4}$$

where $\xi_{inc}(n_g)$ is the correction factor that modifies r_{cr} for

different gas content, such that:

$$\xi_{inc}(n_g) = \frac{2}{3}\cos\left\{\frac{1}{3}\cos^{-1}\left[1-f(n_g)\right]\right\}+\frac{1}{3}, \quad \text{for } 0 \le f(n_g) \le 2. \tag{5}$$

The plot of the coefficient multiplier is shown in figure 1.

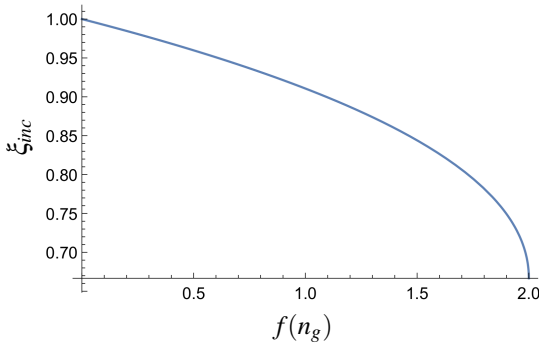

Figure 1: Value of the coefficient multiplier ξ_{inc} for the incipient case as a function of gas content. The solid blue line is obtained from the analytic solution given by (5).

The reduction in the critical activation energy for all the previous cases can also be summarized by the following expression:

$$\begin{aligned}\Delta G^*_{act} &= \xi_{act}(n_g)\left(\frac{16\pi\sigma^3_{\ell g}}{3\Delta p^2_{cr}}\right)\\ &= \xi_{act}(n_g)\Delta G^*_{act,v},\end{aligned} \tag{6}$$

where the variation in the coefficient $\xi_{act}(n_g)$ multiplying $\Delta G^*_{act,v}$ can be expressed as a function of $f(n_g)$ whose analytic solution is given by:

$$\begin{aligned}\xi_{act}(n_g) =& \frac{1}{9}\left[(6\cos\Theta+3\cos 2\Theta-2\sqrt{3}\sin\Theta+\sqrt{3}\sin 2\Theta)\right.\\ &\left.+\frac{4}{3}f(n_g)\ln\left(\frac{1-\cos\Theta+\sqrt{3}\sin\Theta}{1+2\cos\Theta}\right)^3\right],\end{aligned} \tag{7}$$

where $\Theta = (1/3)\cos^{-1}[1-f(n_g)]$. The result of this expression is shown in figure (2).

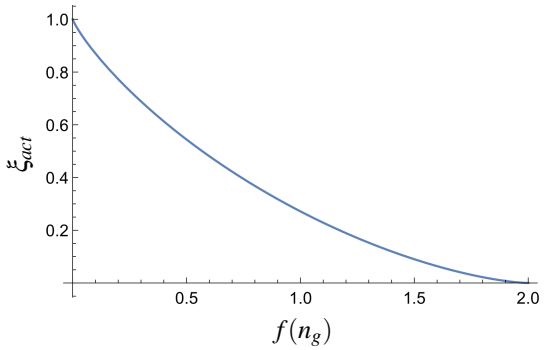

Figure 2: Value of the coefficient multiplier for the critical Gibbs energy required for activation as a function of gas content. The solid blue line is obtained from the analytic solution given by (7).

For the desinent case, we look at the properties of a bubble collapse. The critical radius in this case is an equilibrium radius given by the following expression:

$$r_{eq} = \xi_{des}(n_g)\frac{2\sigma_{\ell g}}{(p_\ell - p_v)}, \tag{8}$$

where $\xi_{des}(n_g)$ is the correction factor that modifies r_{eq} for different gas content, such that: where,

$$\xi_{des}(n_g) = \begin{cases}\frac{2}{3}\cos\left\{\frac{1}{3}\cos^{-1}\left[f(n_g)-1\right]\right\}-\frac{1}{3}, \\ \qquad\qquad \text{if } 0 \le f(n_g) \le 2 \\ \frac{2}{3}\cosh\left\{\frac{1}{3}\cosh^{-1}\left[f(n_g)-1\right]\right\}-\frac{1}{3}, \\ \qquad\qquad \text{otherwise}\end{cases}. \tag{9}$$

The result of the expression is shown in figure (3). It is clear that when no gas is present the equilibrium radius goes to zero, however, when gas is present we get a stable non-zero equilibrium indicating the presence of gas bubbles that can be sustained despite the increase in pressure across the interface.

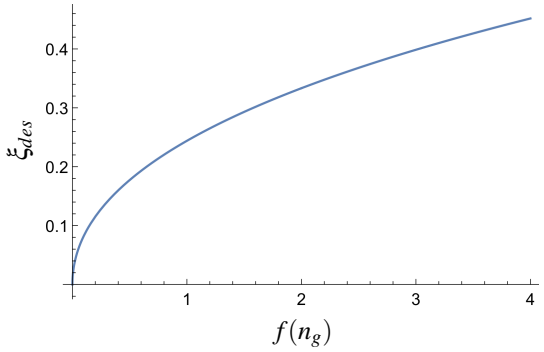

Figure 3: Value of the coefficient multiplier for the desinent case as a function of gas content.

When it comes to cavitation susceptibility meter (CSM) measurement, the diameter of the bubble (d_0) is typically estimated from the critical pressure values registered at cavitation events. The problem is typically solved numerically. The equation is given by the following expression:

$$d_0^3 + \frac{4\sigma_{\ell g}}{(p_{\ell,0} - p_v)} d_0^2 - \frac{4\sigma_{\ell g}}{3(p_{\ell,0} - p_v)} \left[\frac{4\sigma_{\ell g}}{3(p_{\ell,cr} - p_v)} \right]^2 = 0, \tag{10}$$

where it is solved analytically instead. The final solution for the initial bubble diameter is given by:

$$d_0 = \xi_0(n_g) \frac{4\sigma_{\ell g}}{(p_{\ell,0} - p_v)}, \tag{11}$$

where

$$\xi_0(n_g) = \begin{cases} \frac{2}{3}\cos\left\{ \frac{1}{3}\cos^{-1}\left[f(n_g)\left(\frac{p_{\ell,0}-p_v}{p_{\ell,cr}-p_v} \right)^2 - 1 \right] \right\} \\ -\frac{1}{3}, \qquad \text{if } \frac{|p_{\ell,cr}-p_v|}{|p_{\ell,0}-p_v|} \geq \frac{\sqrt{2f(n_g)}}{2} \\ \frac{2}{3}\cosh\left\{ \frac{1}{3}\cosh^{-1}\left[f(n_g)\left(\frac{p_{\ell,0}-p_v}{p_{\ell,cr}-p_v} \right)^2 - 1 \right] \right\} \\ -\frac{1}{3}, \qquad \text{otherwise} \end{cases} \tag{12}$$

The cumulative background nuclei distribution is then estimated as a function of d_0 as shown in figure (4). The experimental data is obtained from Venning et al. (2018) where the tunnel water was degassed to 30% of saturation at atmospheric pressure.

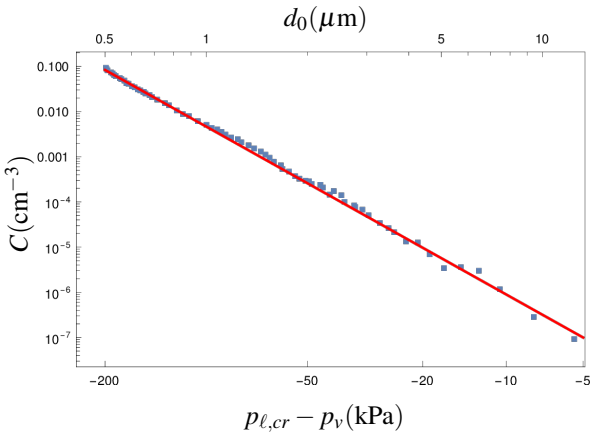

Figure 4: Cumulative background nuclei distribution in the Australian Maritime College (AMC) cavitation tunnel. Trend line drawn in red is a power fit, and the symbols are experimental values. The values for d_0 on the top axis are calculated using (11) with $f(n_g) = 2$, which recovers Blake's assumption.

From first principles, the expression for the cumulative distribution can be written as a function of ΔG^*_{act}:

$$C^* = C_0 \exp\left[-\frac{\Delta G^*_{act}}{kT} \right], \tag{13}$$

such that

$$\frac{\partial C^*}{\partial d_0} = -\frac{18M}{\pi} \exp\left[-\frac{\Delta G^*_{act}}{kT} \right] d_0^{-4}, \tag{14}$$

where $C_0 = M/V$, M being the number of molecules and V the bubble volume. We recover the -4 power law typically observed in experiments (Fig 23 in Khoo et al. (2020)). For more details and plot comparisons, refer to Alamé and Mahesh (2024).

POLYDISPERSE MODEL

Governing equations and numerical method

In large-eddy simulations (LES), large scales are directly accounted for by the spatially filtered Navier–Stokes equations, whereas the effect of small scales is modeled. The spatially filtered incompressible Navier–Stokes equations are as follows:

$$\frac{\partial \overline{u}_i}{\partial t} + \frac{\partial}{\partial x_j}(\overline{u}_i \overline{u}_j) = -\frac{\partial \overline{p}}{\partial x_i} + \nu \frac{\partial^2 \overline{u}_i}{\partial x_j \partial x_j} - \frac{\partial \tau_{ij}}{\partial x_j},$$

$$\frac{\partial \overline{u}_i}{\partial x_i} = 0, \tag{15}$$

where u_i is the velocity, p is the pressure divided by density, ν is the kinematic viscosity, the overbar $\overline{(.)}$ denotes the spatial filter and $\tau_{ij} = \overline{u_i u_j} - \overline{u}_i \overline{u}_j$ is the sub–grid stress. The dynamic Smagorinsky model proposed by Germano et al. (1991) and modified by Lilly (1992) is used to model the subgrid stress terms. The Lagrangian time scale is dynamically computed based on surrogate–correlation of the Germano–identity error (Park and Mahesh, 2009). This approach extended to unstructured grids has shown good performance for a variety of flows (Verma and Mahesh, 2012).

Eq. (15) is solved by a numerical method developed by Mahesh et al. (2004) for incompressible flows on unstructured grids. The algorithm is derived to be robust without any numerical dissipation. It is a finite volume method where the Cartesian velocities and pressure are stored at the centroids of the cells and the face normal velocities are stored independently at the centroids of the faces. A predictor–corrector approach is used. The predicted velocities at the control volume centroids are first obtained and then interpolated to obtain the face normal velocities. The predicted face normal velocity is projected so that the continuity equation in eq. (15) is discretely satisfied. This yields a Poisson equation for pressure which is solved iteratively using a multi–grid approach. The pressure field is used to update the Cartesian control volume velocities using a least–square

formulation. Time advancement is performed using an implicit Crank–Nicholson scheme. The algorithm has been validated for a variety of problems over a range of *Re*.

To account for the vapor phase, a cavitation model has to be included. Here we use an extension to the methodology presented in Brandao and Mahesh (2022) which was developed for the inception regime. In their work, a single transport equation for the vapor phase is computed, which accounts for the entire amount of vapor. Given that the amount of vapor produced in the inception regime is small, the changes in the mixture density is negligible. Thus, the vapor phase is treated as a passive scalar. The original unfiltered transport equation for the vapor phase, neglecting the diffusion term, is

$$\frac{\partial \rho_v \alpha}{\partial t} + \frac{\partial \rho_v \alpha u_j}{\partial x_j} = S, \tag{16}$$

where S is the cavitation source term. The vapor volume fraction is indicated by α, and ρ_v is the vapor density which is assumed to be constant. The model has been validated against the results from a compressible homogeneous mixture model with a preconditioning methodology for the incipient regime in Brandao and Mahesh (2022). The extension we employ here assumes the vapor volume fraction is a polydisperse distribution of bubbles divided discretely into bins of different sizes at different concentrations per unit volume. Polydisperse models (also called population balance models) are not commonly used to simulate cavitating flows. More recently, a comprehensive model was developed by Li and Carrica (2021) that includes bubble coalescence and breakup, and homogeneous and heterogeneous nucleation. The general form of the equation is given as

$$\frac{\partial N_k}{\partial t} + \frac{\partial N_k u_j}{\partial x_j} = \frac{\dot{m}_{k-1/2}}{m_k - m_{k-1}} N_{k-1/2} - \frac{\dot{m}_{k+1/2}}{m_{k+1} - m_k} N_{k+1/2}, \tag{17}$$

where $\dot{m}_{k\pm1/2}$ is the mass transfer term between adjacent bins, and $N_{k\pm1/2}$ is the bubble number density at the edge between bins, which here is taken as the average between N_k and $N_{k\pm1}$ although high order methods are recommended Li and Carrica (2021). The volume fraction of each bin can be written as $\alpha_k = N_k \frac{4\pi {R_k}^3}{3}$, where R_k is the radius of the bubbles in bin k, thus equation (17) can be rewritten as

$$\begin{aligned} \frac{\partial \rho_v \alpha_k}{\partial t} + \frac{\partial \rho_v \alpha_k u_j}{\partial x_j} = & \frac{\dot{m}_{k-1/2}}{m_k - m_{k-1}} N_{k-1/2} \rho_v V_{bk} \\ & - \frac{\dot{m}_{k+1/2}}{m_{k+1} - m_k} N_{k+1/2} \rho_v V_{bk}. \end{aligned} \tag{18}$$

Here, $V_{bk} = \frac{4\pi {R_k}^3}{3}$. The mass transfer term is based on the asymptotic solution of the Rayleigh–Plesset equation and is given by

$$\dot{m}_{k\pm1/2} = 4\pi \rho_v {R^2}_{k\pm1/2} sign(p_v - p) \sqrt{\frac{2}{3} \frac{|p_v - p|}{\rho_l}}, \tag{19}$$

where p_v is the vapor pressure and $R_{k\pm1/2}$ is the limiting radius between adjacent bins. It is evident from equation (18) that the amount of vapor in a bin is determined by the mass transfer between its adjacent bins and that the mass transfer between bins cancel each other out such that mass is conserved. Thus for the last bin, $\dot{m}_{k+1/2} = 0$.

Problem and results

Incompressible large-eddy simulation (using equations 15 to 19) is used to simulate flow over a three-dimensional elliptical hydrofoil at 12 degrees angle of attack and Reynolds number (*Re*) of 9×10^5 based on root chord length and freestream velocity. The simulations are performed at the cavitation number (σ) of 2.1 and are based on the experiments of Boulon et al. (1999). The hydrofoil has a NACA 16–020 cross-section and an elliptical planform of span $S = 0.18\ m$, a root chord length $c = 0.12\ m$ and the aspect ratio is 3.8. The hydrofoil is mounted such that the mid point of the root chord of the hydrofoil is the origin of the Cartesian coordinate system and the tip is located at $(0, -S, 0)$. The hydrofoil span aligns with the y axis and x is the downstream streamwise direction. The two side walls are located at $z = \pm L_z/2$, where $L_z = 0.175\ m$, and the tip-gap is $e = 60\ mm$, is generally chosen as the reference case corresponding to no confinement due to the bottom wall. As stated in the reference paper, the two side walls cause confinement resulting in a 27% increase in lift. The inflow and outflow planes are located at $L_{up} = 2.58c$ upstream and $L_{dn} = 4.92c$ downstream of the tip, respectively. The schematic of the computational domain is shown in figure 5.

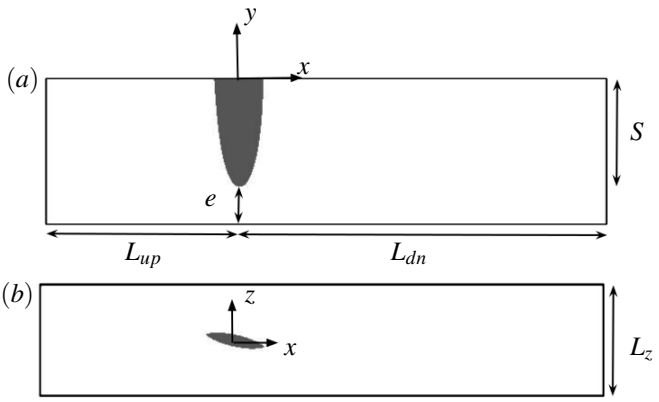

Figure 5: Schematic of the computational domain shown in the planes (a) $z = 0$ and (b) $y = 0.1$.

Freestream velocity is prescribed at the inflow and convective boundary conditions are applied at the outflow.

All other domain boundaries have no–slip boundary conditions. The mesh contains approximately 44 million hexahedral control volumes. The span of the hydrofoil has more than 260 cells and there are more than 400 cells in z direction for the fine grid. The gap between tip of the hydrofoil and the bottom wall contains more than 80 cells. The tip vortex is resolved over more than 20 cells, which is in line with the simulations of hydrofoil tip vortex by Hsiao and Pauley (1998). The grid is clustered near all the wall boundaries with a nominal wall–normal first cell size of $8.3 \times 10^{-4}c$ and $1.67 \times 10^{-3}c$ at hydrofoil surface and other walls respectively with a growth rate of one percent. All the results presented in this section are normalized appropriately using U_∞ and c, except when the units are explicitly mentioned. The flow is taken to be at room temperature, which yields $p_v \approx 2kPa$.

We assume that the bubble distribution ranges from $0.5\mu m$ to $5mm$ and it is divided into 8 bins. The amount of vapor prescribed at the inflow follows the conditions from the water tunnel at the Australian Maritime College investigated in the work of Khoo et al. (2020). Two distributions are studied, named as "natural" and "seeded", corresponding to conditions where the water is poor and rich in nuclei respectively. They are shown in figure 6. It is important to mention that the water can also be called as "strong" or "weak", depending whether the flow is poor or rich in nuclei, respectively. Those distributions yield an overall inflow vapor void fraction of $\alpha \approx 6.1 \times 10^{-15}$ and 1.85×10^{-4} for the natural and seeded cases respectively. The cavitation number is chosen to be $\sigma = 2.1$, which is the critical value reported by Boulon et al. (1999) for the angle of attack and confinement value used in the present work. It is important to mention that the critical cavitation number is defined in Boulon et al. (1999) as the value at which the vapor core attaches to the tip. Thus, the critical σ is lower than the inception σ, which is the value at which the first instance of cavitation is observed. Prior to presenting the results it is important to discuss the criteria used to identify inception. Inception is usually identified by visual or acoustic techniques. Visually, inception is detected when cavitating structures larger than a certain size are observed. Many thresholds have been used in the past. Agarwal et al. (2018) in a experimental study of inception at turbulent shear layers, identified inception when a bubble grows larger than $157\mu m$. In numerical simulations using the Euler–Lagrange framework, Bappy et al. (2022) assumed that inception had occurred when a bubble became larger than $500\mu m$, while Park et al. (2009) used the threshold of $1mm$. When the vapor phase is modeled in a Eulerian framework, the volume fraction is commonly employed as the variable that identifies inception. Cheng et al. (2021), e.g., visualized incipient structures by iso–surfaces of $\alpha = 0.1$. Here, we follow Park et al. (2009) and assume inception occurs when the volume fraction of the last bin, which contains bubbles larger than $1mm$, is greater than 0.001.

Figures 7 and 8 display the iso–surfaces of $\alpha = 0.001$ for bubbles larger and smaller than $1mm$ for the natural and seeded cases, respectively, at an instant of time. Taking the mixture density as the volumetric average between the phases densities, $\rho = \alpha\rho_v + (1-\alpha)\rho_l$, this maximum void fraction would yield a total change in the mixture density of less than 0.1% if a homogeneous mixture approach was used, confirming that it is the incipient regime and that treating the vapor phase as a passive scalar is appropriate. The cavitation topology is very different in each case. In the natural case, inception is found to be an intermittent event confined to the tip vortex at a position close to the hydrofoil's tip. The region undergoing inception is so tiny that it is hard to visualize it in figure 7; therefore, a zoomed view is provided in figure 9. In addition, the concentration of bubbles smaller than $1mm$ does not amount to $\alpha = 0.001$. In the seeded case, cavitation at the tip vortex is fully developed, showing a protuberant structure connected to the hydrofoil's tip. This behavior is consistent with the visual observations from Boulon et al. (1999) at the critical cavitation number. These differences between each case are consistent with experimental observations (Arndt and Maines, 2000) and highlight that the inception cavitation number for the seeded case is much higher than for the natural case. The seeded case also provide some unique features. Given the continuous supply of large nuclei in the freestream, part of the suction side very close to the leading edge of the hydrofoil also experience cavitation. Furthermore, the entire suction side is covered with a layer of bubbles smaller than $1mm$.

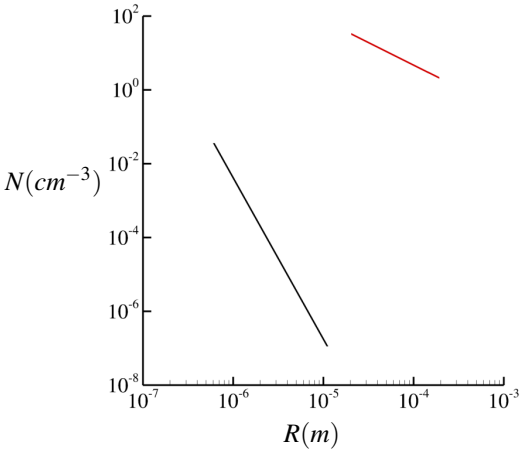

Figure 6: Bubble distribution at inflow for natural (black) and seeded cases (red).

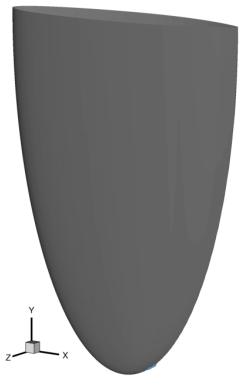

Figure 7: Iso–surfaces of $\alpha = 0.001$ for bubbles larger (blue) and smaller (transparent light gray) than $1mm$ for the natural case.

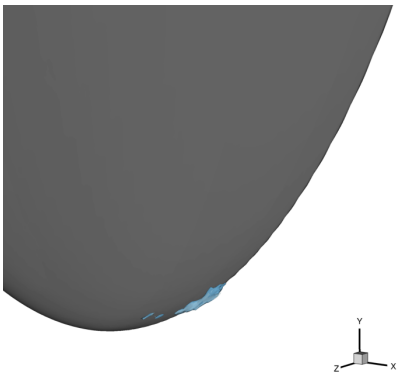

Figure 9: Zoomed view of an iso–surfaces of $\alpha = 0.001$ for bubbles larger than $1mm$ for the natural case.

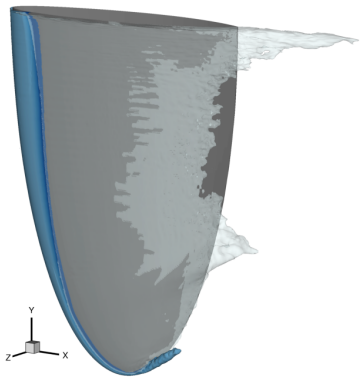

Figure 8: Iso–surfaces of $\alpha = 0.001$ for bubbles larger (blue) and smaller (transparent light gray) than $1mm$ for the seeded case.

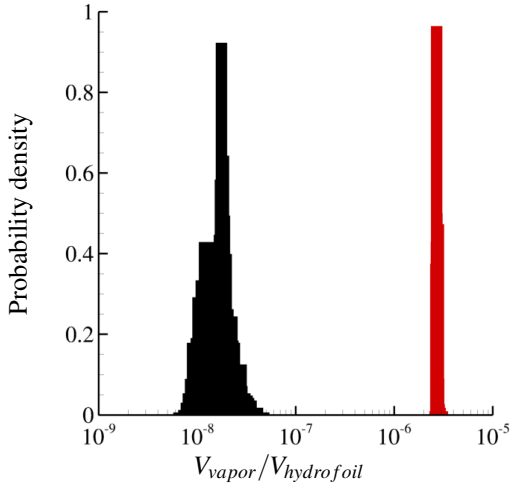

Figure 10: Probability density functions of volume of vapor produced in the natural (black) and seeded case (red) scaled with the volume of the hydrofoil.

The probability density functions (PDF) of the total volume of vapor produced (for bubbles larger than $1mm$) is given in figure 10 for both natural and seeded cases. The seeded case produces a volume of vapor around $O(2)$ larger than the natural case, which is expected. The range of values of volume produced in the natural case is, however, much broader. The difference between the minimum and maximum values is $O(1)$. The amount of vapor produced in the seeded case is almost "fixed" changing very little in time, forming a stable cavity as seen in figure 8.

COMPRESSIBLE HYBRID MODEL

Governing equations (Multi-scale model)

Madabhushi and Mahesh (2023) have developed a compressible multi-scale model where the Eulerian equations govern the homogeneous mixture of liquid and large vapor (or resolved) cavities, and the sub-grid (or unresolved) vapor bubbles are tracked in a Lagrangian sense using $kR-RP$ equation. The important properties and results of the model will be summarized below. The key idea is to split the total vapor mass into constituent resolved and unresolved components as shown below

$$\rho Y_v = \rho Y_{v_{res}} + \rho Y_{v_{un}} \tag{20}$$

were ρ denotes density, Y_v denotes the vapor mass fraction and the subscripts *res* and *un* denote resolved

and unresolved vapor, respectively. Such splitting allows independent treatment of both these length scales where a transport equation governs the resolved vapor and the unresolved bubbles are tracked in Lagrangian sense using the novel $kR-RP$ equation. Substituting equation (20) in the compressible Navier-Stokes equations results in the following set of equations.

$$\begin{aligned} &\frac{\partial Q}{\partial t}+\frac{\partial F_j}{\partial x_j}=-\frac{DQ_{un}}{Dt}-Q_{un}\frac{\partial u_{un_j}}{\partial x_j} \\ &\text{where } Q=\begin{bmatrix}\rho Y_l\\ \rho Y_{lr}u_{lr_i}\\ \rho Y_{res}\end{bmatrix}\quad F=\begin{bmatrix}\rho Y_l u_{lr_j}\\ \rho Y_{lr}u_{lr_i}u_{lr_j}+pn_{x_i}\\ \rho Y_{res}u_{lr_j}\end{bmatrix} \\ &Q_{un}=\begin{bmatrix}0\\ \rho Y_{un}u_{un_i}\\ \rho Y_{un}\end{bmatrix}\text{ and }\ Y_{lr}=Y_l+Y_{res}\end{aligned} \tag{21}$$

where subscripts l refers to liquid and lr refers to the homogeneous mixture of liquid and resolved vapor, u_{lr} is the velocity of the mixture of liquid and resolved vapor, u_{un} denotes the velocity of the sub-grid bubbles and p is the mixture pressure.

The unresolved terms on the right-hand side of the equation (21) act as source terms and represent the effect of sub-grid bubbles on the mixture of liquid and large-scale vapor. The divergence term $(\partial u_{un_j}/\partial x_j)$, which represents the expansion/compression rate, needs to be modelled as standard numerical techniques will be inaccurate due to the poor resolution of the bubbles. It is expressed in terms of the bubble properties as shown below

$$\begin{aligned} &\frac{\partial u_{un_j}}{\partial x_j}=\frac{3\dot{R}}{R} \\ &\rho Y_{v_{un}}\frac{\partial u_{un_j}}{\partial x_j}=\sum_{k=1}^{N}\frac{3\rho_{v_k}\alpha_k\dot{R}_k}{R_k}. \end{aligned} \tag{22}$$

where R_k, $\dot{R}_k$ and ρ_{v_k} denote the radius, velocity and density of the k^{th} bubble. These bubble properties are obtained from the *kR-RP* equation.

The Rayleigh–Plesset equation (or its variants) are generally used to model the spherical motion of the tiny vapor bubbles. These equations are derived assuming that the bubble primarily responds to the ambient pressure (or p_∞). However, the bubble in general is surrounded by other vapor cavities of different shapes and sizes and is often exposed to shock/expansion waves. In other words, the bubble predominantly responds to the local changes in pressure. Hence, the goal is to account for the local effects on the bubble in a consistent manner.

$$\begin{aligned} &\frac{\partial}{\partial r}\left(\frac{\partial\phi}{\partial t}+\frac{1}{2}\left(\frac{\partial\phi}{\partial r}\right)^2\right)=-\frac{1}{\rho}\frac{\partial p}{\partial r}, \\ &\frac{\partial^2\phi}{\partial t^2}=c^2\Delta\phi \end{aligned} \tag{23}$$

The *kR-RP* equation is derived from the spherical momentum and the linear wave equations (equation 23) where ϕ is the velocity potential. The spherical momentum equation is now integrated from the bubble surface ($r=R$) to a finite distance ($r=kR$) rather than $r=\infty$, where k is a constant parameter. Substituting the general solution of ϕ and the boundary conditions in the momentum equation results in the following equation.

$$\begin{aligned} &R\ddot{R}\left(1-\frac{1}{k}-\frac{\dot{R}}{c}\right)+\frac{3}{2}\dot{R}^2\left(1-\frac{4}{3k}-\frac{1}{3k^4}-\frac{\dot{R}}{3c}\right) \\ &\quad=\frac{1}{\rho}\left(1+\frac{\dot{R}}{c}+\frac{R}{c}\frac{\partial}{\partial t}\right)(p_b-2\sigma/R-4\mu\dot{R}/R-p(kR_i)) \\ &\quad-\frac{1}{2}\left(\frac{\dot{R}}{c}+\frac{R}{c}\frac{\partial}{\partial t}\right)\frac{\dot{R}^2}{k^4}-\frac{2\dot{R}^3+6R\dot{R}\ddot{R}+R^2\dddot{R}}{kc}+I \end{aligned} \tag{24}$$

where p_b is the bubble pressure, σ is the surface tension and μ is the dynamic viscosity. $p(kR)$ (pressure at a finite distance kR from the bubble centre) is now the external pressure acting on the bubble. The term I models the inter-bubble interaction among the sub-grid bubbles. Equation 24 is referred to as the *kR-RP* equation. For derivation details, please refer to Madabhushi and Mahesh (2023).

Key features of the multi-scale model

Firstly, we demonstrate the ability of the model to capture both large-scale and sub-grid vapor behavior accurately. We consider a single vapor bubble subjected to a higher ambient pressure. Two cases are chosen as shown below

$$\begin{aligned} &\text{Resolved Bubble: } R_0/\Delta x=50;\ P_\infty/P_0=50 \\ &\text{Unresolved Bubble: } R_0/\Delta x=0.5;\ P_\infty/P_0=50 \end{aligned} \tag{25}$$

where R_0, Δx and P_0 are the initial bubble size, cell size and initial bubble pressure, respectively. For both cases, the ambient pressure is $P_\infty=1$ atm. Figure (11) shows the comparison of the bubble size between the multi-scale model and the reference *RP* ODE. For both unresolved and resolved bubbles (figures 11*a* and 11*b*), the size and the collapse time agree well with the reference solution.

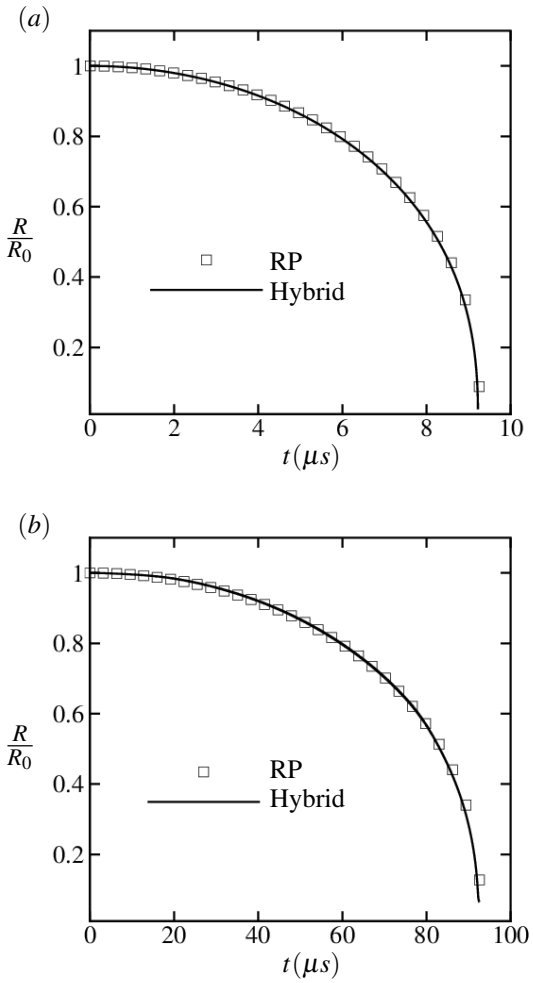

Figure 11: Bubble size (non-dimensional) comparison between the multi-scale model and the *RP* ODE when the bubble is (a) fully resolved and (b) sub-grid.

We also consider a case where both large and sub-grid bubbles co-exist. Following is the problem setup

$$\begin{aligned} &\text{Resolved Bubble: } R_{1_0} = 1 \text{ mm}; \;\; R_{1_0}/\Delta x = 25 \\ &\text{Unesolved Bubble: } R_{2_0} = 0.1 \text{ mm}; \;\; R_{2_0}/\Delta x = 1.25 \end{aligned} \tag{26}$$

The initial pressure (P_0) for both the bubbles is 0.5 atm. The ambient pressure (P_∞) is 1 atm. As the bubbles begin to collapse, the larger one generates pressure waves that propagate towards the smaller bubble (figure 12, impacting its oscillatory motion. Conversely, the sub-grid bubble has a negligible impact because of its smaller size. Figure 12(a) shows the comparison of the size of the sub-grid bubble for the current case and when it is isolated. The oscillations decay at a faster pace for the current case, which can be attributed to the pressure waves produced by the large bubble.

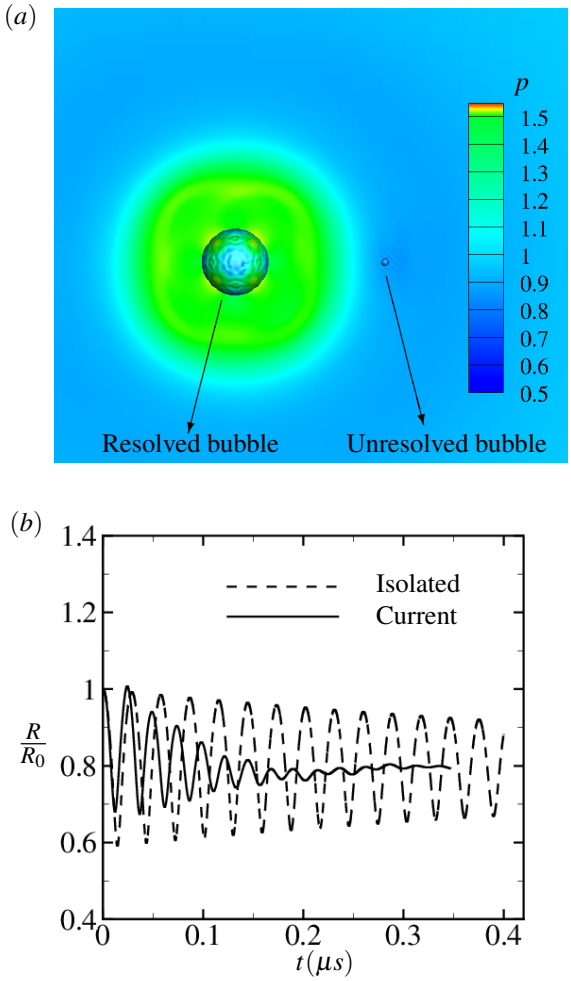

Figure 12: (a) Instantaneous snapshot of the pressure wave generated by the resolved bubble. Iso-contour of volume fraction (colored with pressure) is used to represent the bubbles: $\alpha = 0.65$ for the resolved bubble and $\alpha = 0.015$ for the unresolved bubble. (b) Comparison of the size of the unresolved bubble between the current scenario and when it is isolated.

Hybridization of the multi-scale model

In the previous section, we demonstrated the ability of the multi-scale model to capture both large and sub-grid vapour length scales accurately. However, there exist scenarios where the vapor cavity can collapse from an initially large size to a very small size and vice versa. Capturing such dynamics requires a transition between the Eulerian and Lagrangian frameworks. We extend the multi-scale model to account for such transition based on the bubble size to cell-size ratio.

Equation (20) (the splitting of the total vapor mass) is modified as shown below

$$\begin{aligned} \rho Y_v &= (1-\beta)\rho Y_{v_{res}} + \beta \rho Y_{v_{un}} \\ \text{Hence } \rho &= \rho Y_l + (1-\beta)\rho Y_{v_{res}} + \beta \rho Y_{v_{un}} \end{aligned} \tag{27}$$

where the subscripts l, *res* and *un* denote liquid, resolved vapor and unresolved vapor respectively. β is the transition parameter that lies between 0 and 1 and indicates whether the vapor is in Eulerian or Lagrangian frame.

$$\begin{aligned}
&\beta = 0 : \text{Fully resolved (Eulerian)} \\
&\beta = 1 : \text{Fully unresolved (Lagrangian)} \\
&0 < \beta < 1 : \text{Transition between Eulerian and Lagrangian}
\end{aligned} \tag{28}$$

We choose a hyperbolic tangent profile for β for a smooth transition, as defined below

$$\beta = \left(1 - tanh\left(max\left(\frac{R/h - k_1}{k_2}, 0\right)\right)\right) \tag{29}$$

where R - Bubble radius, h - cell size, k_1 and k_2 are constant parameters. k_1 is the threshold at which transition is initiated and k_2 is a measure of transition rate. R is obtained from the $kR-RP$ equation for the sub-grid bubbles. For resolved cavities, R is defined as follows

$$R = V_b^{1/3}; \;\; V_b = \sum_{\substack{icv=1 \\ \alpha_i > 0.01}}^{N} \alpha_i V_i \tag{30}$$

where V_b - Bubble volume, α_i - vapor volume fraction in the i^{th} cell and V_i - volume of the i^{th} cell.

Problem setup and Results

We consider the oscillation of a gas bubble initially subjected to a lower external pressure. Following are the initial conditions

$$R_0 = 50\mu m; \;\; Pb_0 = 10\text{atm}; \;\; P_{amb} = 1\text{atm}; \;\; R_0/h = 2.0 \tag{31}$$

where R_0 and Pb_0 are the initial bubble radius and pressure, respectively. P_{amb} denotes the ambient pressure and h is the computational cell size. The dimensions of the domain are $L_x = L_y = L_z = 100R_0$. The initial free-stream volume fraction is $1e-4$. For this case $k_1 = 5$ and two values of k_2 are chosen, $k_2 = 0.01$ and 0.03.

The accurate exchange of mass and momentum between the Lagrangian and Eulerian frameworks plays a key role in conserving the gas mass and momentum and, hence, the accurate evolution of the bubble properties. Figures 13(a) and 13(b) depict the temporal changes in net gas mass under two conditions: (a) when the resolved and unresolved components are not in mechanical equilibrium, and (b) when they are in mechanical equilibrium, i.e. $p_{lr} = p_{un}$.

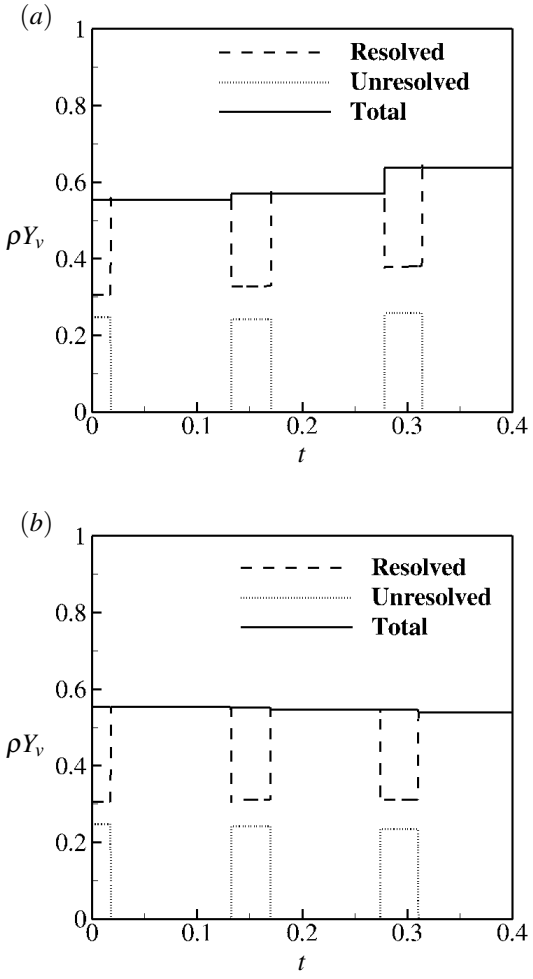

Figure 13: Net gas mass when the resolved and unresolved components are (a) not in mechanical equilibrium and (b) assumed to be in mechanical equilibrium.

The solid, dashed and dotted lines represent the net gas mass, net resolved gas mass and net unresolved gas mass in the entire domain, respectively. Initially, the bubble is sub-grid; hence, the net unresolved gas mass (dotted line) is non-zero. As the bubble expands, its radius crosses the threshold (k_1), initiating the transfer of mass and momentum from the Lagrangian to the Eulerian framework. Hence, the net unresolved mass drops to zero ($t \sim 0.02$). Subsequently, as the bubble reaches its maximum radius and begins to collapse, its size falls below the threshold, initiating a reverse transfer from the Eulerian to the Lagrangian framework (approximately at $t \sim 0.13$), resulting in a non-zero value for unresolved mass. This process continues, and we observe the second Euler-Lagrangian transition around $t = 0.3$.

In case (a), the net vgas mass experiences an increase,

whereas it remains conserved in case (b). Notably, this increase occurs during the Eulerian to Lagrangian transition. When the resolved and unresolved gas pressures are not assumed to be in equilibrium, their velocities can differ. Consequently, during the transition, the mass flux of each of them will be different, leading to either the accumulation or depletion of net gas mass. However, in case (b), due to the assumption of mechanical equilibrium, the net gas mass remains conserved, with changes less than 0.5%.

We also compute the bubble radius variation for case (b), shown in figure 14. The horizontal dashed line at $R/R_0 = 2.5$ indicates the transition point. We observe a good agreement between the hybrid model and the reference analytical solution. We notice a slight jump in radius at $t \sim 0.2$ and $t \sim 0.33$ during the Lagrangian to Eulerian transition. This could be attributed to the definition of bubble radius in the Eulerian framework, which will be addressed in further studies.

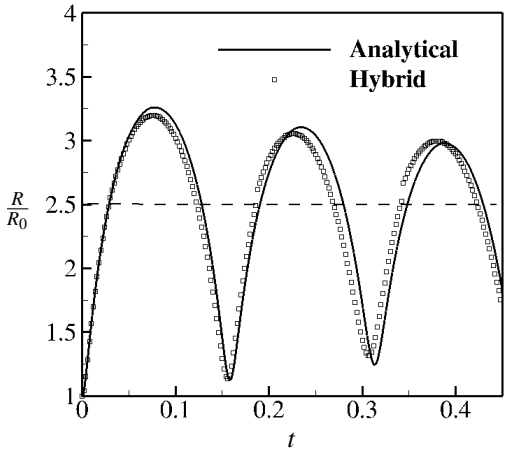

Figure 14: Comparison of the non-dimensional bubble radius
between the hybrid model and the reference analytical solution.

Another important requirement for the hybrid model is ensuring a smooth transition, free from spurious oscillations in the bubble pressure. To address this, we choose two distinct values of k_2: $k_2 = 0.01$ and $k_2 = 0.03$. Figure 15(a) illustrates the evolution of bubble pressure for both cases, with the point of contention being the Eulerian-Lagrangian transition, highlighted by circles. For a closer examination, Figure 15(b) provides a zoomed-in view of the bubble pressure at time instance B, with the solid line representing $k_2 = 0.01$ and square symbols representing $k_2 = 0.03$. At around $t \sim 0.28$, noticeable pressure fluctuations are evident for $k_2 = 0.01$. However, these fluctuations are significantly smaller for $k_2 = 0.03$, indicating that a relatively slower transition rate is preferable for achieving a smoother transfer process.

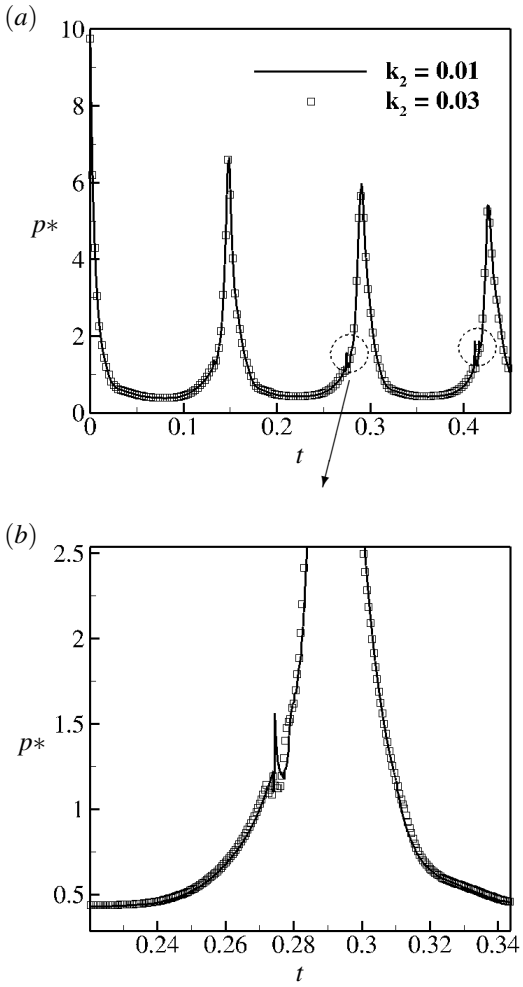

Figure 15: (a) Bubble pressure evolution for $k_2 = 0.01$ and $k_2 = 0.03$ where $p*$ is the non-dimensional pressure. (b) Magnified view of the pressure at $t \sim 0.28$ (indicated by the arrow).

SUMMARY

In this work, we investigate the effect of non-condensable gas on cavitation and develop models for inception and fully developed cavitation regimes. Firstly, we use a Gibbs-free energy approach to quantify the effect of gas on inception. The gas content is found to reduce the energy barrier for nucleation. Analytical expressions for critical radius and activation energy are derived as a function of the gas content. We also derive an analytical expression for the initial bubble diameter as a function of critical pressure, which is typically used in CSM measurements. A model for the cumulative bubble distribution is proposed which is shown to predict the -4

power law.

In the inception regime, we developed a polydisperse model and applied it to study the cavitation inception near the tip of NACA 16-020 elliptic hydrofoil, based on the experiments conducted by Boulon et al. (1999). We chose two initial distributions of vapor nuclei, 'natural' and 'seeded, ' representing conditions where water is poor and rich in nuclei, respectively. In the natural case, intermittent inception events were observed close to the hydrofoil tip. However, cavitation is fully developed for the seeded case, with a protuberant structure connected to the hydrofoil tip. Notably, the volume of vapour in the seeded case is almost $O(2)$ larger and remains constant in time, whereas the natural case produced a range of volume values.

Finally, we proposed an extension to the multi-scale model of Madabhushi and Mahesh (2023) to incorporate hybridization. A hyperbolic tangent profile is chosen for the transition function (β) to ensure a smooth transition. The transition process is governed by two important parameters, k_1 and k_2, which determine the transition threshold and the transition rate, respectively. The model has been validated for the case of oscillation of a gas bubble. The total vapor mass remained conserved when the constituent phases were assumed to be in mechanical equilibrium. We also investigated the effect of k_2 on spurious pressure oscillations during the transition and observed that a relatively higher value of k_2 produces very minimal oscillations in pressure.

ACKNOWLEDGEMENTS

This work is supported by the United States Office of Naval Research under Grants ONR N00014–17-1–2676 and ONR N00014-14-1-0290 with Dr. Ki–Han Kim and Dr. Yin-Lu Young as the program managers. Computing resources were provided by the Minnesota Supercomputing Institute (MSI) and the High-Performance Computing Modernization Program (HPCMP).

REFERENCES

Agarwal, K., Ram, O., and Katz, J. "Cavitating structures at inception in turbulent shear flow". In Proceedings of the 10th International Symposium on Cavitation (CAV2018), 2018.

Alamé, K. and Mahesh, K. "Effect of gas content on cavitation nuclei". J. Fluid Mech., 982:A4, 2024.

Arndt, R. E. A. and Maines, B. H. "Nucleation and bubble dynamics in vortical flows". Journal of Fluids Engineering, 122:488–493, 2000.

Bappy, M. H., Carrica, P. M., Li, J., Martin, J. E., Vela-Martin, A., Freire, L. S., and Buscaglia, G. C. "A sub-grid scale cavitation inception model". Physics of Fluids, 34(3):033308, 2022.

Becker, R. and Döring, W. "Kinetische behandlung der keimbildung in übersättigten dämpfen". Annalen der physik, 416(8):719–752, 1935.

Bensow, R. E. and Bark, G. "Implicit les predictions of the cavitating flow on a propeller". J. Fluids Eng., 132: 1–10, 2010.

Bernath, L. "Theory of bubble formation in liquids.". Industrial & Engineering Chemistry, 44(6):1310–1313, 1952.

Bhatt, M. and Mahesh, K. "Numerical investigation of partial cavitation regimes over a wedge using large eddy simulation". International Journal of Multiphase Flow, 122:103155, 2020.

Blake, F.G. "The tensile strength of liquids: a review of the literature. technical memo no. 9". 1949.

Blander, M. and Katz, J.L. "Bubble nucleation in liquids". AICHE Journal, 21(5):833–848, 1975.

Boulon, O., Callenaere, M., Franc, J.-P., and Michel, J.-M. "An experimental insight into the effect of confinement on tip vortex cavitation of an elliptical hydrofoil". Journal of Fluid Mechanics, 390:1–23, 1999.

Brandao, F. L. and Mahesh, K. "Large–eddy simulation of cavitation inception in a shear flow". International Journal of Multiphase Flow, 146:103865, 2022.

Budich, B., Schmidt, S. J., and Adams, N. A. "Numerical simulation and analysis of condensation shocks in cavitating flow". J. Fluid Mech., 838:759–813, 2018.

Carey, V.P. Liquid-vapor phase-change phenomena: an introduction to the thermophysics of vaporization and condensation processes in heat transfer equipment. CRC Press, 2020.

Chen, J.L., Xue, B., Mahesh, K., and Siepmann, J.I. "Molecular simulations probing the thermophysical properties of homogeneous ly stretched and bubbly water systems". J. Chem. Eng. Data, 64(9):3755–3771, 2019.

Cheng, H., Long, X., Ji, B., Peng, X., and Farhat, M. "A new euler–lagrangian cavitation model for tip–vortex cavitation with the effect of non–condensable gas". International Journal of Multiphase Flow, 134:103441, 2021.

Cole, R. "Boiling nucleation". In Advances in heat transfer, volume 10, pages 85–166. Elsevier, 1974.

Farkas, L. "The velocity of nucleus formation in supersaturated vapors". Z. phys. Chem, 125:236–242, 1927.

Frenkel, J. Kinetic theory of liquids. Dover, New York, 1955.

Gao, Z., Wu, W., and Wang, B. "The effects of nanoscale nuclei on cavitation". J. Fluid Mech., 911, 2021.

Germano, M., Piomelli, U., Moin, P., and Cabot, W. H. "A dynamic subgrid-scale eddy viscosity model". Physics of Fluids A, 3(7):1760–1765, 1991.

Gibbs, J.W. Scientific Papers of J. Willard Gibbs, in Two Volumes, volume 1. Longmans, Green, 1906.

Gnanaskandan, A. and Mahesh, K. "A numerical method to simulate turbulent cavitating flows". International Journal of Multiphase Flows, 70:22–34, 2015.

Hsiao, C. T. and Pauley, L. L. "Numerical study of the steady–state tip vortex flow over a finite–span hydrofoil". Journal of Fluids Engineering, Transactions of the ASME, 120(2):345–353, 1998.

Hsiao, C-T., Chahine, G. L., and Liu, H-L. "Scaling effect on prediction of cavitation inception in a line vortex flow". Journal of Fluids Engineering, 125:53–60, 2003.

Khoo, M. T., Venning, J. A., Pearce, B. W., Takahashi, K., Mori, T., and Brandner, P. A. "Natural nuclei population dynamics in cavitation tunnels". Experiments in Fluids, 61(2):1–20, 2020.

Li, J. and Carrica, P. "A population balance cavitation model". International Journal of Multiphase Flow, 138: 103617, 2021.

Lienhard, J.H. and Karimi, A. "Homogeneous nucleation and the spinodal line". 1981.

Lilly, D. K. "A proposed modification of the Germano subgrid–scale closure model". Physics of Fluids A, 4:3: 633–635, 1992.

Madabhushi, A. and Mahesh, K. "A compressible multi-scale model to simulate cavitating flows". Journal of Fluid Mechanics, 961:A6, 2023.

Maeda, N. Nucleation of gas hydrates. Springer, 2020.

Mahesh, K., Constantinescu, G., and Moin, P. "A numerical method for large-eddy simulation in complex geometries". J. Comput. Physics, 197(1): 215–240, 2004.

Menzl, G., Gonzalez, M.A., Geiger, P., Caupin, F., Abascal, J.L.F., Valeriani, C., and Dellago, C. "Molecular mechanism for cavitation in water under tension". PNAS, 113(48):13582–13587, 2016.

Park, K., Seol, H., Choi, W., and Lee, S. "Numerical prediction of tip vortex cavitation behavior and noise considering nuclei size and distribution". Applied Acoustics, 70:674–680, 2009.

Park, N. and Mahesh, K. "Reduction of the Germano–identity error in the dynamic Smagorinsky model". Physics of Fluids (1994-present), 21(6): 065106, 2009.

Skripov, V.P. Metastable Liquids. John Wiley and Sons, 1974.

Venning, J. A, Khoo, M. T, Pearce, B. W, and Brandner, P. A. "Background nuclei measurements and implications for cavitation inception in hydrodynamic test facilities". Exp. Fluids, 59:1–4, 2018.

Verma, A. and Mahesh, K. "A Lagrangian subgrid–scale model with dynamic estimation of Lagrangian time scale for large eddy simulation of complex flows". Physics of Fluids, 24(8):085101, 2012.

Volmer, M. and Weber, A. "Keimbildung in übersättigten gebilden". Zeitschrift für physikalische Chemie, 119 (1):277–301, 1926.

Zeldovich, Y.B. "On the theory of new phase formation: cavitation". Acta Physicochem., USSR, 18:1, 1943.

DISCUSSION

Jin-Keun Choi,
Naval Surface Warfare Center Carderock Division (872), 9500 MacArthur Blvd, West Bethesda, MD 20817, Ph: (301)227-5952, email: jinkeun.choi.civ@us.navy.mil

The authors thank you for your comments and questions, which are addressed below.

1. *What is $kR-RP$ and what differentiates it from the typical Rayleigh-Plesset equation approaches?*
   A brief overview of the $kR-RP$ equation is provided on page 8. For further details on the derivation and key assumptions, please refer to section 2.3 of Madabhushi and Mahesh (2023).

2. *In Figure 7, analysis was done for two groups: bubbles larger and smaller than 1 mm. Why is 1 mm chosen and is there any physical or experimentally observed reason to group by this size?*
   The reason for choosing 1 mm has been mentioned on page 6 (highlighted in red).

3. *In the presented framework, the resolved vapor is handled by the Eulerian transport equation, while the unresolve vapor is handled by the Lagrangian kR-RP solver. The surface tension is likely included in the kR-RP naturally, but how the surface tension is considered in the transport equation approach? Could the different ways of considering the surface tension be the reason behind the small discontinuity in Figure14 and Figure 15?*
   Currently, surface tension is considered only in the $kR-RP$ equation. The small discontinuity in figure 15 could possibly be due to the definition of bubble radius in the Eulerian system. It is obtained from the volume fraction field based on a certain threshold ($\alpha > 0.01$ for the current case). This is still a work in progress, and the precise definition of the size of an Eulerian cavity will be addressed.

4. *In the hybridization section, the transition parameter β (equations 25 and 26) is used to make smooth transition between the resolved and unresolved vapor. However, it looks like both Eulerian and Lagrangian equations are "always" solved, and the parameter β is used to provide a weighted average value to some state variables. There would be a way to minimize duplicated computation, how did or would the authors minimize this redundancy for computational efficiency?*
   Currently, both the Eulerian and Lagrangian equations are solved during the transition ($0 < \beta < 1$). The current goal is to develop a consistent and accurate hybridization approach. As the framework evolves, we will address the efficiency issues.

5. *Regarding the discussion of mechanical equilibrium vs. non-equilibrium about Figure 13, why did the authors consider non-equilibrium case? Isn't the resolved and unresolved vapor just the two descriptions of the same bubble? Then the pressure of the two should be equal to each other. What is the physical meaning of non-equilibrium here? In Figure 13(b), there is slight loss of vapor at the Lagrangian to Eulerian transitions (t = 0.17, 0.31); what do the authors think the reason?*
   The key idea in developing this framework is to allow sub-grid bubbles to have a different pressure than the surrounding liquid and resolved cavities. However, during the transition, the pressure should be the same as the Eulerian and Lagrangian are two descriptions of the same bubble. Hence, the mechanical equilibrium assumption is invoked when sub-grid bubbles grow to the order of cell size.

6. *Considering the definition of β in equation 27, one may think that the ideal values of k_1 and k_2 are k_1 = about 2 (i.e. bubble diameter is the cell size) and k_2 = about 1 (i.e. when bubble diameter is 1.5 times the cell size, then $\beta = 0.24$, a quarter way from the fully resolved)? Could the authors discuss any issues or experiences if these parameters are too tight or too loose?*
   k_1 represents the transition threshold and k_2 is a measure of the transition rate. Both are independent parameters. In our experience, a small value of k_2 (~ 0.01) would introduce pressure oscillations during the transition. k_2 of $0.03-0.05$ was found to give small to negligible oscillations. For k_1, the appropriate value was found to be between $4-6$. $k_1 < 3$ would imply that the Eulerian cavity would have a coarse resolution during the transition. Large value of k_1 implies that the bubble is assumed to be spherical despite growing significantly, which may not necessarily be true all the time, especially if it undergoes deformation.

DISCUSSION

Anonymous,

The authors thank you for your comments and questions, which are addressed below.

1. *The title sounds too broad.*
   The authors believe the title is justified as the models developed and presented in this paper are for different regimes of cavitation.

2. *These three parts seem to be simply collected for this paper. It will be good if the authors justifies why these three are put together here.*
   The goal of this paper is to present the novel models developed for different cavitation regimes. These models can be integrated into the main code/solver in the future, enabling simulations of a wide range of complex cavitating flows.

3. *Could the authors elaborate on their idea for the definition?*
   The definition of the bubble radius in the Eulerian frame is mentioned on page 10, equation 30.

DISCUSSION

Anonymous,

The authors thank you for your comments and questions, which are addressed below.

1. *Recommend modifying the title*
   The authors believe the title is justified as the models developed and presented in this paper are for different regimes of cavitation.

2. *Summary of major findings?*
   The summary of the major findings is discussed under the 'Summary' section on page 12.

3. *Many terms here are undefined (pages 2,3,7 and 8*)?
   These terms have been defined clearly and highlighted in red.

4. *How about the work of Bryngelson and Chahine (for the hybrid model)?*
   Bryngelson has developed an Euler Lagrangian model, not a hybrid model. Chahine has developed a hybrid model, but using incompressible equations. The current hybrid model is developed using the compressible governing equations.

5. *Graphic should be improved. Why do you have partial boarders on all the graphs (figure 1)*
   The plot has been modified.

6. *Why such large value (1mm in polydisperse model)?*
   The reason for choosing 1 mm has been mentioned on page 6 (highlighted in red).

7. *Please carefully go over full paper. Many grammatical mistakes and incomplete sentences.*
   The grammatical mistakes and incomplete sentences have been corrected.

8. *The different pieces are not connected together.*
   The goal of this paper is to present and discuss the novel models developed for different cavitation regimes. These models can be integrated into the in-house solver, enabling simulations of a wide range of complex cavitating flows.

DISCUSSION

Anonymous,

This is a very good paper. I look forward to seeing the tools used in the future and a great talk at SNH.
The authors thank you for your comments and look forward to presenting this work at SNH.